universe

MDPI

Article

The Applicability of the Averaged Transition Probability of Neutrino Oscillation in Astrophysics

Paul Chong Wa Lai [1,2]

[1] Mullard Space Science Laboratory, University College London, Holmbury St. Mary, Surrey RH5 6NT, UK; chong.wa.lai@rwth-aachen.de
[2] Institute for Theoretical Particle Physics and Cosmology, RWTH Aachen University, Sommerfeldstraße 16, D-52074 Aachen, Germany

Abstract

High-energy astrophysical neutrinos are predominantly produced through charged-pion decay, yielding a flavour ratio of $f_e : f_\mu : f_\tau = 1/3 : 2/3 : 0$ at the source. During propagation, neutrino oscillations modify this composition, and the flavour ratio measured at Earth is commonly expected to correspond to the oscillation-averaged value. Deviations from this standard picture are typically interpreted as signatures of new physics in the neutrino sector or alternative production mechanisms at the source. However, before invoking physics beyond the standard picture, it is essential to establish the validity of the conventional prediction itself. In this work, we review and quantify the conditions under which the oscillation-averaged transition probability is applicable, thereby laying the groundwork for future studies of astrophysical neutrino flavour ratios.

Keywords: neutrino oscillation; neutrino astronomy; high-energy astrophysics

1. Introduction

Neutrinos come in three flavours—the electron, muon, and tau neutrinos (ν_e, ν_μ, ν_τ). When neutrinos travel in vacuum or some medium, the composition of their flavours changes, a phenomenon known as neutrino oscillation. By measuring the neutrino flavour composition of a certain source at a certain distance, we can study the neutrino oscillation properties, such as the mixing angles [1], and/or the neutrino production mechanisms of the emitting sources (e.g., [2]). For example, for terrestrial neutrino production sites, such as accelerators and nuclear reactors, we have excellent understanding of the neutrino production mechanism and also a precise measurement of the distance between the source and the detector, such that we can measure the oscillation properties with great precision (e.g., [3–5]). Another example is the solar neutrinos, which enable us to derive the neutrino properties and also to verify our understandings of neutrino production processes happening inside the Sun (e.g., [6–9]).

Thanks to current neutrino observatories such as IceCube [10–12] and Super-Kamiokande [13], and also future observatories such as IceCube-Gen2 [14], KM3NeT [15], Baikal-GVD [16], P-ONE [17], HUNT [18], TRIDENT [19], NEON [20], and Hyper-Kamiokande [21], the applications of astrophysical neutrinos are receiving more attention from astrophysicists and particle physicists. Studies of astrophysical neutrino flavour ratio can be mainly divided into two directions: (1) to study the fundamental properties of neutrinos, and (2) to study the physical processes happening in the astrophysical environments. Despite many downsides to study astrophysical neutrinos such as poor distance

Check for updates

Academic Editor: Oleksandr Tomalak

Received: 20 October 2026
Revised: 10 November 2026
Accepted: 13 November 2026
Published: 16 November 2026

Copyright: © 2026 by the author. Licensee MDPI, Basel, Switzerland. This article is an open access article distributed under the terms and conditions of the Creative Commons Attribution (CC BY) license.

measurements and uncertain neutrino production mechanisms, the large distance between the source and the detector provides a unique opportunity to probe the oscillation or propagation properties in a different regime, and test frontier theoretical models which effects only become detectable when the neutrino travels for a long distance, such as Lorentz invariance violation and quantum gravity [22,23]. On the other hand, if we assume that the neutrino oscillation property does not alter for large distance propagation in the astrophysical environment, the measured neutrino flavour ratio can help verify the neutrino production mechanisms at the source.

For high-energy astrophysical neutrinos ($\gtrsim$GeV), the consensus is that they are predominantly produced in pion decays (e.g., [24–27]). Pions are produced when high-energy cosmic rays collide with a photon or a nucleus. A negatively charged pion will shortly decay into a muon and a muon antineutrino. The muon will then decay into an electron, an electron antineutrino, and a muon neutrino, i.e.,

$$\pi^- \to \mu^- + \bar{\nu}_\mu \to e^- + \bar{\nu}_e + \nu_\mu + \bar{\nu}_\mu \,. \tag{1}$$

The final products contain one electron neutrino and two muon neutrinos and are the same for positively charged pions (counting both neutrinos and antineutrinos). Given the neutrino flavour ratio at production is $f_e : f_\mu : f_\tau = 1/3 : 2/3 : 0$, the predicted flavour ratio measured at Earth is very close to equipartition, which corresponds to the oscillation-averaged value (see Section 2). Indeed, current measurements of the ratio of the astrophysical neutrino background are consistent with the equipartition expectation [2]. However, specific scenarios could lead to a flavour ratio different from the equipartition, which require observations of better sensitivity to test these models. From the production perspective, muon-damping and neutron decays could result in a production flavour ratio different from $f_e : f_\mu : f_\tau = 1/3 : 2/3 : 0$ and thus a different flavour ratio at the detection sites [28–31]. From the oscillation perspective, theoretical models such as physics beyond the standard model or Lorentz violation could change the oscillation properties and thus predict a different measured flavour ratio [32–34]. In order to test the non-conventional theories, it is essential to establish a solid foundation for the conventional model, such that when more precise measurements become available, the result can be correctly interpreted.

In this article, we revisit the reasons behind the conventional equal-ratio flavour prediction and quantify the necessary conditions that lead to this result. Most of the media through which astrophysical neutrinos propagate, such as the interstellar medium, the circumgalactic medium, and the intergalactic medium, typically have very low number densities ($n_{\rm H} \lesssim 1\,{\rm cm}^{-3}$), such that matter effects can be neglected. However, astrophysical neutrinos may encounter much denser environments either shortly after their production or during propagation, where matter effects may become significant. Examples include the interiors of stars and the Earth. In this work, we restrict our consideration to neutrino propagation in vacuum-like media, while the effects of matter are left for future studies. Unless specified, all the neutrino oscillation calculations are performed using the following parameter values taken from Ref. [1]: $\Delta m^2_{21} = 7.49 \times 10^{-5}\,{\rm eV}^2$, $\Delta m^2_{31} = 2.513 \times 10^{-3}\,{\rm eV}^2$, $\theta_{12} = 33.68^\circ$, $\theta_{23} = 43.3^\circ$, $\theta_{13} = 8.56^\circ$, and $\delta_{\rm CP} = 212^\circ$, in which the normal mass ordering (NO) is assumed. We adopt the Planck units where $c = \hbar = 1$.

2. Standard Neutrino Oscillation Formula and Flavour Equipartition

The classical neutrino oscillation formula is given by

$$P^{\rm std}_{\alpha\beta}(L,E) = \Re\left[\sum_{j,k} U^*_{\alpha j} U_{\beta j} U_{\alpha k} U^*_{\beta k} \exp\left(-i\frac{\Delta m^2_{jk} L}{2E}\right)\right] \tag{2}$$

or, more explicitly

$$P^{\mathrm{std}}_{\alpha\beta}(L,E) = \delta_{\alpha\beta} - 4\sum_{j>k}\Re(U^*_{\alpha j}U_{\beta j}U_{\alpha k}U^*_{\beta k})\sin^2\left(\frac{\Delta m^2_{jk}L}{4E}\right) + 2\sum_{j>k}\Im(U^*_{\alpha j}U_{\beta j}U_{\alpha k}U^*_{\beta k})\sin\left(\frac{\Delta m^2_{jk}L}{2E}\right) \quad (3)$$

Ref. [35], where $\alpha,\beta = e,\mu$, or τ, $j,k = 1,2$, or 3, $P_{\alpha\beta}$ is the probability of detecting neutrino with flavour β given the original neutrino flavour α, $U_{\alpha i}$ is the Pontecorvo-Maki-Nakagawa-Sakata matrix (PMNS matrix) [1], $\Delta m^2_{jk} = m^2_j - m^2_k$, m_j is the mass of the neutrino mass eigenstate j, L is the distance travelled by the neutrino, and E is the energy of the neutrino. The oscillation length is therefore given by $L^{\mathrm{osc}}_{jk} = (4\pi E)/\Delta m^2_{jk}$. Equation (3) consists of periodic functions only, such that we can define the averaged transition probability $P^{\mathrm{ave}}_{\alpha\beta}$ by taking the average of all the oscillating functions, i.e., $\langle\sin x\rangle = 0$ and $\langle\sin^2 x\rangle = 1/2$. Therefore, we obtain

$$P^{\mathrm{ave}}_{\alpha\beta} = \delta_{\alpha\beta} - 2\sum_{j>k}\Re(U^*_{\alpha j}U_{\beta j}U_{\alpha k}U^*_{\beta k})\,. \quad (4)$$

The importance of which will become clear later. From Equation (3), it appears that the neutrino flavour ratio is distance-dependent, implying that astrophysical neutrino sources at different distances would be observed with different flavour ratios. However, this formula is not directly applicable to realistic settings because it is based on the plane-wave approximation and the limitations of measurements are not taken into account. We will show in Section 3 that, under certain conditions, Equation (3) reduces to Equation (4).

In the case that Equation (4) can be applied, we can connect the neutrino flavour ratio at source $(f^0_e, f^0_\mu, f^0_\tau)$ to the ratio observed $(f^{\mathrm{obs}}_e, f^{\mathrm{obs}}_\mu, f^{\mathrm{obs}}_\tau)$ through the matrix defined in Equation (4):

$$\begin{bmatrix} f^{\mathrm{obs}}_e \\ f^{\mathrm{obs}}_\mu \\ f^{\mathrm{obs}}_\tau \end{bmatrix} = \begin{bmatrix} 0.549 & 0.215 & 0.236 \\ 0.215 & 0.407 & 0.378 \\ 0.236 & 0.378 & 0.386 \end{bmatrix} \begin{bmatrix} f^0_e \\ f^0_\mu \\ f^0_\tau \end{bmatrix} \quad . \quad (5)$$

For pion decay with $f^0_e : f^0_\mu : f^0_\tau = 1/3 : 2/3 : 0$, Equation (5) yields $f^{\mathrm{obs}}_e : f^{\mathrm{obs}}_\mu : f^{\mathrm{obs}}_\tau \approx 0.33 : 0.34 : 0.33$. As for the inverted mass ordering (IO; parameter values taken from Ref. [1]), we obtain $f^{\mathrm{obs}}_e : f^{\mathrm{obs}}_\mu : f^{\mathrm{obs}}_\tau \approx 0.32 : 0.34 : 0.34$. Regardless of the choice of the mass ordering, the result is in close agreement with equipartition. In the following, we discuss several conditions under which the reduction from Equation (3) to Equation (4) is expected to hold for astrophysical observations.

3. Measurements of Astrophysical Neutrino Flavour Ratios

In the following, we discuss several mechanisms that may cause the measured flavour ratio to deviate from the standard prediction given by Equation (3) under realistic astrophysical and experimental conditions. These mechanisms can be divided into three categories. In Section 3.1, we investigate effects intrinsic to neutrino propagation. In Section 3.2, we discuss effects related to the physical properties of the neutrino-emitting source. Finally, in Section 3.3, we examine effects arising from experimental limitations. Although most of these mechanisms have been discussed in previous studies, they are often treated only qualitatively, without a comprehensive assessment of the conditions under which they become relevant, or without being considered specifically in the context of astrophysical neutrinos (e.g., [36–41]). In this work, we provide a comprehensive and quantitative analysis of these mechanisms and demonstrate their applicability to astrophysical systems.

3.1. Neutrino Oscillation—Wave-Packet Treatment

The standard neutrino oscillation formula (Equation (3)) is derived under the plane-wave approximation, which is valid when the wave packets of the three neutrino mass

eigenstates sufficiently overlap. A more realistic description of a neutrino is a wave packet with a characteristic size σ_x, rather than a plane wave extending over the entire space. When a neutrino of a given flavour is produced, it is composed of three mass eigenstates, which propagate at slightly different group velocities due to their mass differences. If the neutrino propagates over a sufficiently large distance, the three mass eigenstates will become completely separated, and the interference between them ceases, such that the flavour composition will no longer oscillate during propagation. Quantitatively, neutrino detection becomes incoherent when $\Delta v_{jk} t \gg \sigma_x$, which can be rewritten as $ct \approx L \gg E^2 \sigma_x / \Delta m^2_{jk}$. Ref. [36] shows that a Gaussian wave packet of size σ_x modifies the neutrino oscillation formula as follows:

$$P^{\mathrm{wp}}_{\alpha\beta}(L,E) = \delta_{\alpha\beta} - 2\sum_{j>k} \Re(U^*_{\alpha j} U_{\beta j} U_{\alpha k} U^*_{\beta k}) + 2\Re\left[\sum_{j>k} U^*_{\alpha j} U_{\beta j} U_{\alpha k} U^*_{\beta k} \exp\left(-i\frac{\Delta m^2_{jk} L}{2E}\right) \times \exp\left[-\left(\frac{L}{L^{\mathrm{coh}}_{jk}}\right)^2\right]\right]. \quad (6)$$

with

$$L^{\mathrm{coh}}_{jk} = \frac{4\sqrt{2}E^2}{|\Delta m^2_{jk}|}\sigma_x\,, \quad (7)$$

where L^{coh}_{jk} is the coherence length beyond which the neutrino cannot be coherently detected. Substituting the values of Δm^2_{21} and Δm^2_{31}, we obtain $L^{\mathrm{coh}}_{31} \approx 0.7\,\mathrm{kpc}\,(E/1\,\mathrm{GeV})^2(\sigma_x/1\,\mathrm{cm})$ and $L^{\mathrm{coh}}_{21} \approx 25\,\mathrm{kpc}\,(E/1\,\mathrm{GeV})^2(\sigma_x/1\,\mathrm{cm})$. As analysed in Ref. [38], the spread of wave packets does not change the conditions for decoherence and thus Equation (6) still applies even when the spread is considered.

The size of neutrino wave packets depends on the production process [36,42]. In general, neutrinos produced in denser environments have smaller wave packets, as the parent particles are confined to a narrower region of space. The size of a neutrino produced in pion decay in vacuum can be approximated as $\sigma_x \sim \tau_\pi/\gamma_\pi \sim 10\,\mathrm{m}/\gamma_\pi \sim 0.3\,\mathrm{m}\,(E_\nu/1\,\mathrm{GeV})^{-1}$, where τ_π is the mean lifetime of charged pions, γ_π is the Lorentz factor of the decaying pion, and $E_\pi \sim 4E_\nu$ [43]. Similarly, the size of a neutrino produced in muon decay in vacuum is approximately $\sigma_x \sim \tau_\mu/\gamma_\mu \sim 10^3\,\mathrm{m}/\gamma_\mu \sim 20\,\mathrm{m}\,(E_\nu/1\,\mathrm{GeV})^{-1}$, where τ_μ is the mean lifetime of muons, γ_μ is the Lorentz factor of the decaying muon, and $E_\mu \sim 3E_\nu$. From the above estimation, we find that even when the three neutrinos produced in the pion decay and the subsequent muon decay have similar energies, the size of their wave packets can differ by two orders of magnitude. In contrast, the wave packet size of a neutrino produced in the dense environment of a supernova is estimated to be in the range 10^{-16}–10^{-11} m [36,38,44,45], much smaller than those from decays of free particles. The plausible values of σ_x thus span many orders of magnitude. Direct experimental measurements of neutrino wave packet sizes are challenging. One of the first such measurements constrained the spatial extent of a neutrino produced in beryllium-7 decay to be at least 6.2 pm [46]. Figure 1 illustrates the regimes in L and E under which neutrino detection becomes incoherent, with $\sigma_x = 1\,\mathrm{pm}$ and $\sigma_x = 0.3\,\mathrm{m}\,(E_\nu/1\,\mathrm{GeV})^{-1}$ to represent neutrinos produced in dense environments and pion decay in vacuum, respectively. Low-energy neutrinos reach the incoherent regime at shorter propagation lengths, as the difference in group velocities between mass eigenstates is larger at lower energies. Different classes of neutrino sources are indicated by the shaded regions, and the implications for astrophysical neutrinos are discussed in Section 4.

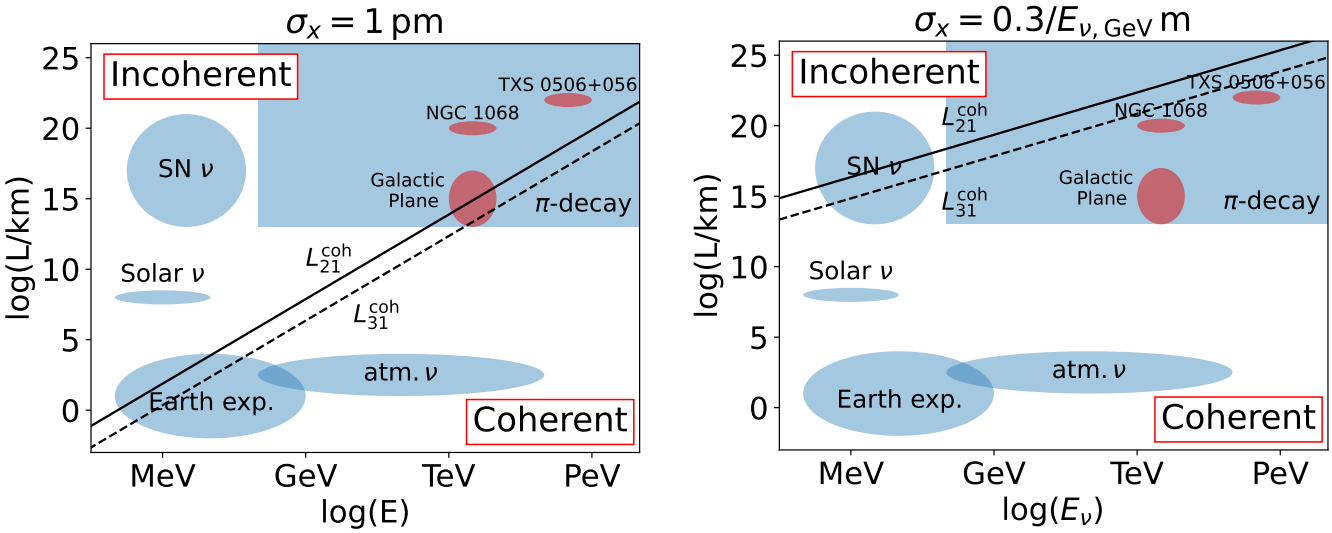


Figure 1. The $L_{21}^{\rm coh}$ (black solid line) and $L_{31}^{\rm coh}$ (black dashed line) lines divide the plots into two regions, where the lower right corner represents the coherent regime and the upper left corner represents the incoherent regime. To keep the plots clean, the $L_{32}^{\rm coh}$ line is omitted because its value is similar to $L_{31}^{\rm coh}$. The lines of transition depend on the size of the neutrino wave packet where we pick $\sigma_x = 1\,\text{pm}$ (**left**) and $\sigma_x = 0.3\,(E_\nu/1\,\text{GeV})^{-1}\,\text{m}$ (**right**) as illustration. In the same plots, the blue shaded regions show the main classes of detectable neutrinos, including neutrino experiments on Earth (e.g., reactors and accelerators), atmospheric neutrinos, solar neutrinos, supernova (SN) neutrinos and neutrinos from pion decay. In particular, the red shaded regions show the rough locations of the identified astrophysical neutrino sources in this plot, including the Galactic Plane, NGC 1068, and TXS 0506+056.

In Figure 2, we show an example of neutrino oscillation in which the coherence length is considered, with $\sigma_x = 1\,\text{pm}$ and $E = 1\,\text{MeV}$. The interference between ν_3-ν_1 and ν_3-ν_2 are first damped after L surpasses $L_{31}^{\rm coh}$ and $L_{32}^{\rm coh}$ ($L_{31}^{\rm coh} \approx L_{32}^{\rm coh}$). When $L \gtrsim 10\,\text{km}$, only ν_1 and ν_2 are still interfering such that only one frequency mode can be observed. When $L \gg L_{21}^{\rm coh}$, the neutrino becomes completely incoherent and no oscillation can be observed. Mathematically, when $L \gg L_{jk}^{\rm coh}$, the exponential term in Equation (6) is damped. In the limit $L \gg L_{jk}^{\rm coh}$, the result coincides with the average transition probability $P_{\alpha\beta}^{\rm ave}$ introduced in Equation (4).

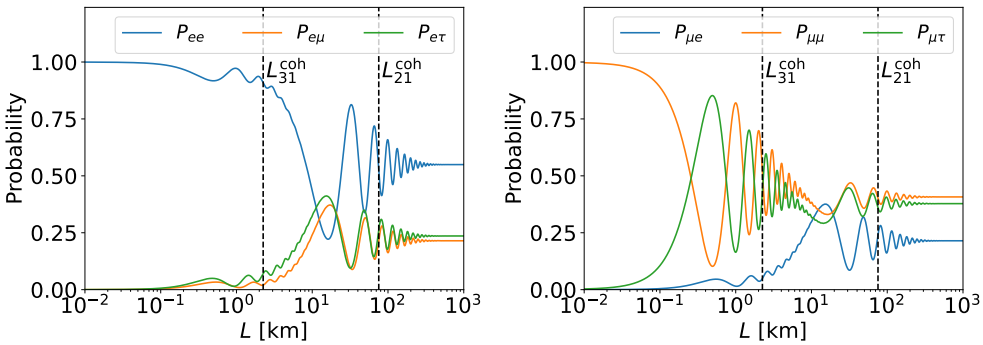


Figure 2. *Cont.*

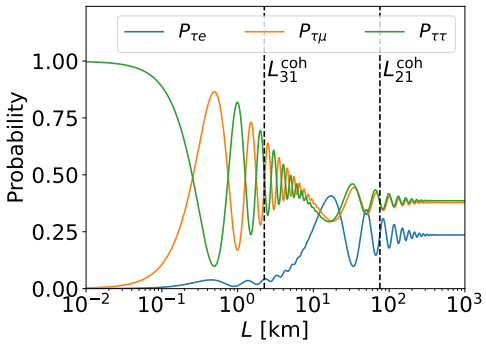


Figure 2. The transition probability when the neutrino is treated as a wave packet. These plots are calculated using Equation (6), with $\sigma_x = 1\,\text{pm}$ and $E = 1\,\text{MeV}$. The transition probability converges to $P^{\text{ave}}_{\alpha\beta}$ at large L. The following oscillation parameters are adopted: $\Delta m^2_{21} = 7.49 \times 10^{-5}\,\text{eV}^2$, $\Delta m^2_{31} = 2.513 \times 10^{-3}\,\text{eV}^2$, $\theta_{12} = 33.68^\circ$, $\theta_{23} = 43.3^\circ$, $\theta_{13} = 8.56^\circ$, and $\delta_{\text{CP}} = 212^\circ$ (NO) [1].

3.2. Size of the Neutrino Source and Its Radial Motion

In this section, we discuss how certain properties of the neutrino source affect the measured neutrino flavour ratio. We consider that the neutrino-emitting source has a finite size ΔL, rather than being a hypothetical point source. We also assume that this neutrino-emitting region is transparent to the emitted neutrinos, meaning that neutrinos do not interact with this region in any way. Since the detector does not distinguish between neutrinos travelled for different distances, neutrinos emitted at different locations within the zone are integrated together in the measurement, such that the measured transition probability is modified into

$$\langle P^{\text{std}}_{\alpha\beta}(L,E)\rangle_{\phi_L} = \int_{L_0}^{L_0+\Delta L} \mathrm{d}L' P^{\text{std}}_{\alpha\beta}(L',E)\phi_L(L')\,, \tag{8}$$

where $\phi_L(L')$ is the weight function that describes the emissivity distribution of the neutrino source. In the simplest case where the emission is spatially uniform, we have $\phi_L(L) = 1/\Delta L$. With $\phi_L(L) = 1/\Delta L$, Equation (8) can be solved analytically

$$\begin{aligned}\langle P^{\text{std}}_{\alpha\beta}(L,E)\rangle^{\text{uni}}_{\phi_L} &= \delta_{\alpha\beta} - 2\sum_{j>k}\Re(U^*_{\alpha j}U_{\beta j}U_{\alpha k}U^*_{\beta k}) \\ &+ 2\Re\sum_{j>k} U^*_{\alpha j}U_{\beta j}U_{\alpha k}U^*_{\beta k}\frac{i2E}{\Delta m^2_{jk}\Delta L}\exp\left(-i\frac{\Delta m^2_{jk}L_0}{2E}\right)\left[\exp\left(-i\frac{\Delta m^2_{jk}\Delta L}{2E}\right)-1\right].\end{aligned} \tag{9}$$

Figure 3 shows the neutrino oscillation pattern when the finite size of the neutrino emitter is taken into account. Here we set $L_0/E = 4\pi/\Delta m^2_{21}$ such that $P_{ee} : P_{e\mu} : P_{e\tau} \approx 1 : 0 : 0$ at $\Delta L = 0$. The value of L_0/E determines the flavour ratio at $\Delta L = 0$ and we also note that Equation (9) is periodic in L_0/E. The choice of L_0/E is not particularly important for the discussion here because we are primarily interested in the large-ΔL regime in which the result is independent of the value of L_0/E, as will be shown below. When ΔL is small, the result reduces to the standard oscillation formula for point-like emitter and detector. As ΔL becomes comparable to L^{osc}_{31} and L^{osc}_{32}, the flavour composition begins to deviate from the standard picture, as the oscillation modes associated with ν_1-ν_3 and ν_2-ν_3 mixing are washed out by the finite size of the emitter. As ΔL increases further and becomes comparable to L^{osc}_{21}, the oscillations between ν_1 and ν_2 are also averaged out. In the limit $\Delta L \gg L^{\text{osc}}_{jk}$, all oscillation modes are averaged out and the measured flavour composition reaches a stable value. Mathematically, this is because the third term on the right hand side of Equation (9) vanishes when ΔL is large.

Due to the low detection rate of neutrinos, neutrino detectors usually accumulate data for a long period of time. If the neutrino source has a radial velocity, its position is constantly

changing throughout the observation, which could result in a modified transition probability similar to a finite-size neutrino emitter described above. The most common type of radial velocity is the recession velocity caused by cosmological expansion. In the low redshift limit, we have $v_r \approx zc$, where v_r is the recession velocity and z is the redshift. The distance receded within an observational period $t_{\rm obs}$ is $v_r t_{\rm obs} \sim 10^{12}\,{\rm km}\,(z/0.01)(t_{\rm obs}/10\,{\rm yr})$. If $v_r t_{\rm obs} \gg L^{\rm osc}_{jk}$, the measured transition probability can be approximated by the averaged formula.

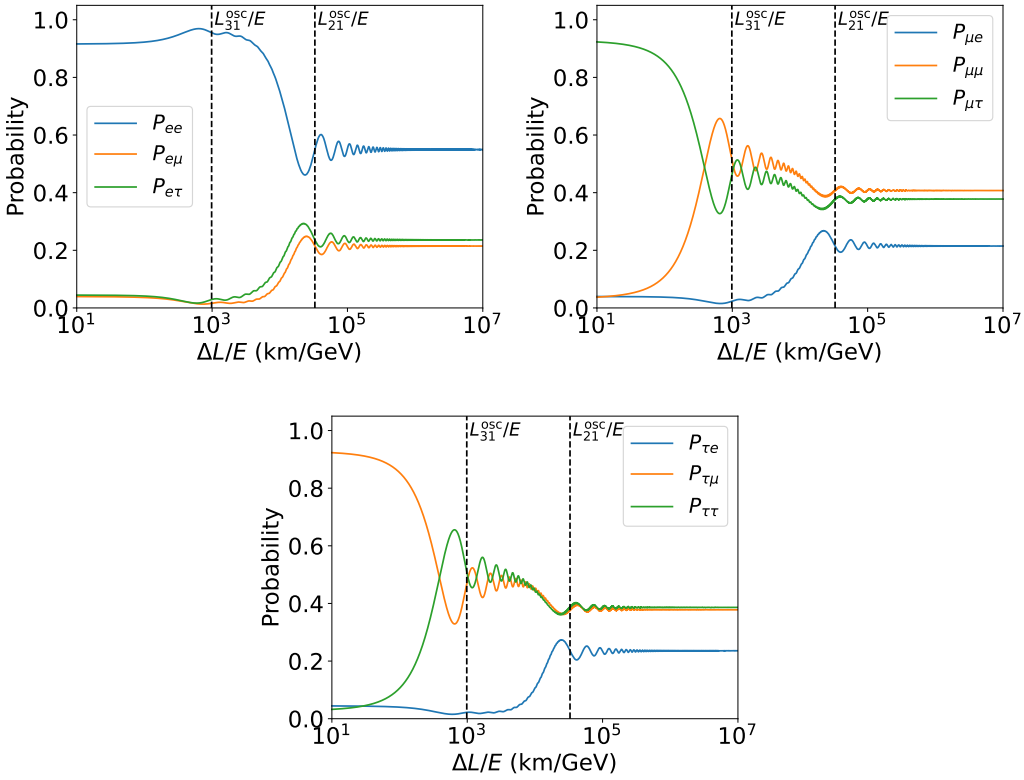


Figure 3. The transition probability when considering the size of the neutrino emitted. These plots are calculated using Equation (9) with $L_0/E = 4\pi/\Delta m^2_{21}$. The transition probability converges to $P^{\rm ave}_{\alpha\beta}$ at large $\Delta L/E$. The following oscillation parameters are adopted: $\Delta m^2_{21} = 7.49 \times 10^{-5}\,{\rm eV}^2$, $\Delta m^2_{31} = 2.513 \times 10^{-3}\,{\rm eV}^2$, $\theta_{12} = 33.68^\circ$, $\theta_{23} = 43.3^\circ$, $\theta_{13} = 8.56^\circ$, and $\delta_{\rm CP} = 212^\circ$ (NO) [1].

3.3. Detection: The Spatial Extent of Detectors and the Energy Bandwidth of Data

In this section, we discuss two aspects of a measurement that could change the observed flavour ratio—the size of detectors and the energy bandwidth of data[1]. We model their effects as follow:

$$\langle P^{\rm std}_{\alpha\beta}(L,E)\rangle_{\phi^D_L,\phi_E} = \int\int {\rm d}L'{\rm d}E' P^{\rm std}_{\alpha\beta}(L',E')\phi^{\rm D}_L(L')\,\phi_E(E')\,, \tag{10}$$

where $\phi^{\rm D}_L(L')$ and $\phi_{\rm E}(E')$ are the normalised weight functions related to the position-dependent detection efficiency and the energy bandwidth effect, respectively. Neglecting $\phi_{\rm E}(E')$ for the moment, it can be seen that Equation (10) has the same mathematical structure as Equation (8). Therefore, the analysis and conclusion made in Section 3.2 can be directly transferred to the size of detectors. That is, if the size of a detector is much larger than the oscillation length, the transition probability can be approximated by the averaged transition probability. Below, we focus on the effect of the energy bandwidth.

The energy-dependent weight function $\phi_E(E')$ consists of two parts, the detector's response $\phi^{\rm D}_E(E')$ and the neutrino energy spectrum of the source $F_\nu(E)$, i.e., $\phi_E(E') \propto F_\nu(E')\phi^{\rm D}_E(E')$. The function has to be normalized such that $\int {\rm d}E'\,\phi_E(E') = 1$. We first consider the simplest case where the neutrino spectrum is flat (${\rm d}F_\nu/{\rm d}E = 0$) and the response

function is uniform for neutrinos with energies in between $E_{\min}$ and $E_{\max}$ ($\mathrm{d}\phi_E^{\mathrm{D}}/\mathrm{d}E = 0$). For mathematical convenience, $E_{\min}$ and $E_{\max}$ are parameterised to be $E_{\min} = E_0/(1+\eta)$ and $E_{\max} = E_0(1+\eta)$, where $\eta \geq 0$. Noted that $\Delta E = E_{\max} - E_{\min}$, Equation (10) becomes

$$\langle P^{\mathrm{std}}_{\alpha\beta}(L,E)\rangle^{\mathrm{uni}}_{\phi_E} = \frac{1}{\Delta E}\int_{E_0/(1+\eta)}^{E_0(1+\eta)} \mathrm{d}E'\, P^{\mathrm{std}}_{\alpha\beta}(L,E')\,. \tag{11}$$

Before diving into the analytical or numerical results, we first predict what we would expect. When the energy bandwidth is narrow, i.e., $\eta \approx 0$, Equation (11) simply recovers the standard oscillation formula. When the energy bandwidth becomes larger, the integral essentially averages over the oscillatory function (reminded that $P^{\mathrm{std}}_{\alpha\beta}$ contains only sine functions), which leads to a result similar to the averaged transition probability $P^{\mathrm{ave}}_{\alpha\beta}$. The condition that marks this transition is when $\Delta m^2_{jk}L/(2E_{\min}) - \Delta m^2_{jk}L/(2E_{\max}) = 2\pi$, namely when the integral is over one cycle. The above condition can be rewritten into $\eta \approx \eta^{\mathrm{crit}}_{jk} \equiv L^{\mathrm{osc}}_{jk}(E_0)/L$. However, since the integrals in Equation (11) looks something like $\int \sin(1/E)\,\mathrm{d}E$, the width of each cycle is not the same, so it does not exactly average out even when ΔE is large. Moreover, when E exceeds a certain value, the sine function does not even behave as an oscillating function. This happens when $\Delta m^2_{jk}L/(2E_{\max}) < 2\pi$, which can be rewritten as $\eta > 1/\eta^{\mathrm{crit}}_{jk}$. When E is sufficiently large, terms that contain $\sin(\Delta m^2_{jk}L/2E)$ or $\sin^2(\Delta m^2_{jk}L/2E)$ all vanish, leaving only the Kronecker delta function (see Equation (3)). This is because neutrinos with higher energy have longer oscillation length. If the propagation distance is shorter than the oscillation length, these neutrinos do not oscillate significantly before reaching the detector. If ΔE is wide enough that includes many neutrinos with very high energy, the integral will be dominated by these non-oscillating neutrinos that Equation (11) results in a Kronecker delta function.

Base on the above analysis, we can categorise the results of Equation (11) into different regimes. In the small η limit where $\eta \ll \eta^{\mathrm{crit}}_{jk}$, it results in the standard oscillation formula. In the large η limit where $\eta \gg 1/\eta^{\mathrm{crit}}_{jk}$, it results in a Kronecker delta function. In the middle regime where η is in between $\eta^{\mathrm{crit}}_{jk}$ and $1/\eta^{\mathrm{crit}}_{jk}$, we have to further divide it into two scenarios: (1) $\eta^{\mathrm{crit}}_{jk} < 1$ or $\eta^{\mathrm{crit}}_{jk} < 1/\eta^{\mathrm{crit}}_{jk}$ and (2) $\eta^{\mathrm{crit}}_{jk} \geq 1$ or $\eta^{\mathrm{crit}}_{jk} \geq 1/\eta^{\mathrm{crit}}_{jk}$. In the first scenario, the energy resolution is neither too small to be ignored nor too large to be dominated by high-energy neutrinos. This results in the averaging of the oscillating function in Equation (11), which results in approximately the averaged transition probability $P^{\mathrm{ave}}_{\alpha\beta}$. In the second scenario, the energy resolution is somewhat small but it extends over to the high-energy, non-oscillating neutrinos. These two factors compete with each other and the result can only be computed numerically. A more detailed explanation of the above analysis can be found in Appendix A.

Figure 4 shows the electron neutrino transition probability as a function of η. We consider six cases with $L/E_0 = (4\pi/\Delta m^2_{21}) \times N$, where $N = 10^3, 10^2, 10^1, 1, 10^{-1}$, and 10^{-2}. The value of L/E_0 is chosen such that the flavour ratio at $\eta = 0$ satisfies $P_{ee} : P_{e\mu} : P_{e\tau} \approx 1 : 0 : 0$ for all values of N. In the first three cases, corresponding to Figure 4a–c, we have $\eta^{\mathrm{crit}}_{jk} < 1$, and the three regimes predicted above are clearly identifiable. Of particular interest is the intermediate regime, in which the transition probability is well approximated by $P^{\mathrm{ave}}_{\alpha\beta}$. A larger L/E_0, or equivalently a smaller $\eta^{\mathrm{crit}}_{jk}$, results in a broader intermediate regime with a more stable averaged value (see Figure 4a,b). In comparison, in Figure 4c, where $\eta^{\mathrm{crit}}_{21} = 0.1$, the intermediate 'platform' is relatively narrow and the oscillation amplitude is considerably larger. Figure 4d corresponds to the transitional case where $\eta^{\mathrm{crit}}_{21} = 1$, in which the intermediate platform no longer exists. For larger values of $\eta^{\mathrm{crit}}_{jk}$, the intermediate regime reduces to a transitional region connecting the small-η and large-η limits.

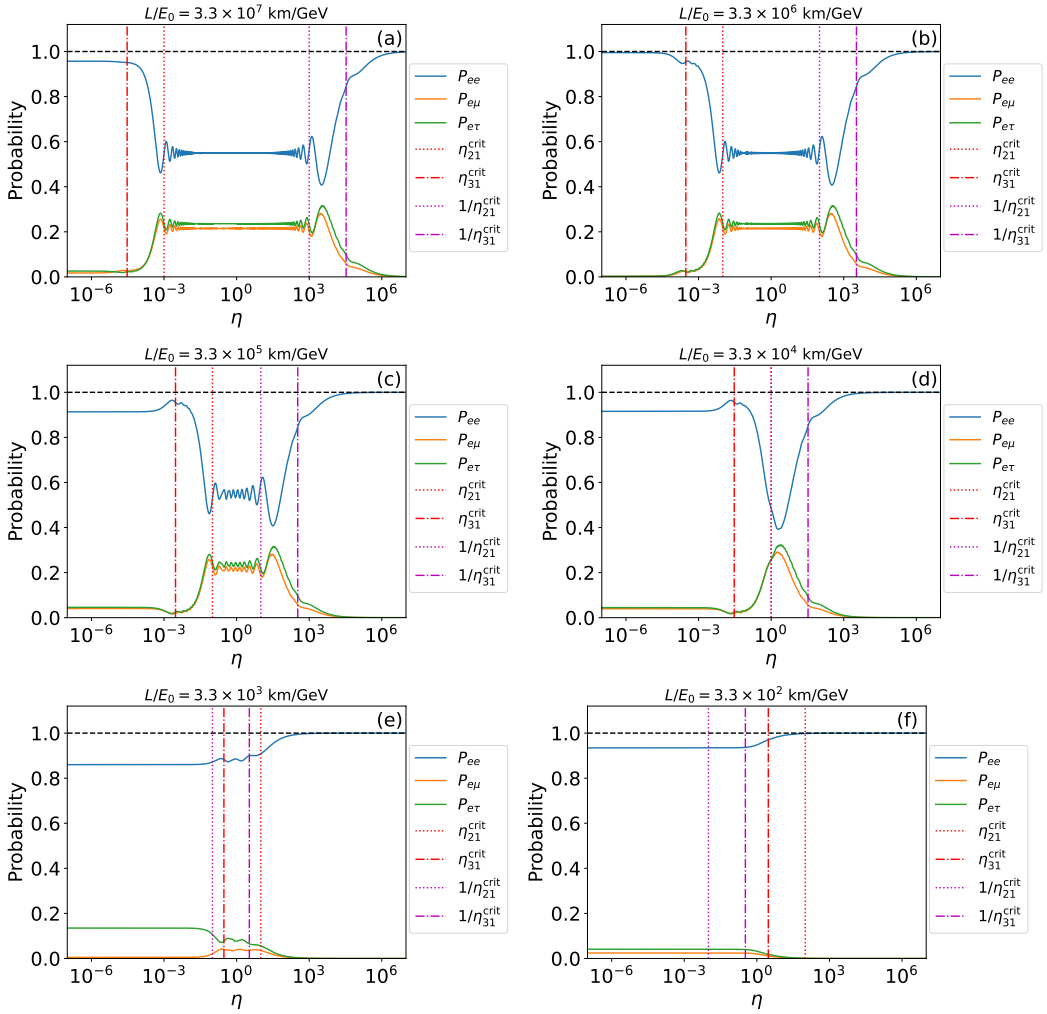


Figure 4. The transition probability when considering the energy bandwidth of a measurement. The neutrino spectrum is assumed to be flat. These plot are calculated using Equation (11). (**a**–**f**) correspond to different values of L/E_0 as shown in each panel. The relatively flat platform in (**a**–**c**) corresponds to the values of averaged transition probability $P_{\alpha\beta}^{\rm ave}$. The following oscillation parameters are adopted: $\Delta m_{21}^2 = 7.49 \times 10^{-5}\,{\rm eV}^2$, $\Delta m_{31}^2 = 2.513 \times 10^{-3}\,{\rm eV}^2$, $\theta_{12} = 33.68^\circ$, $\theta_{23} = 43.3^\circ$, $\theta_{13} = 8.56^\circ$, and $\delta_{\rm CP} = 212^\circ$ (NO) [1].

In the above calculation, we assumed that the neutrino source has a flat spectrum that extends to infinite energy. In reality, a neutrino source typically emits more low-energy neutrinos than the high-energy ones. The most common functional form for a particle spectrum is a power law. We perform the same calculation with $F_\nu \propto E^{-p}$ and the results are shown in Figures 5 and 6, where $p = 2$ and $p = 3$, respectively. The results do not change dramatically for small η, but differ significantly for large η. The most noticeable result is that the transition probability converges to $P_{\alpha\beta}^{\rm ave}$ even at large η. This is because the contribution from high-energy neutrinos are suppressed due to the power-law spectrum. Implications of these calculations are discussed in Section 4.

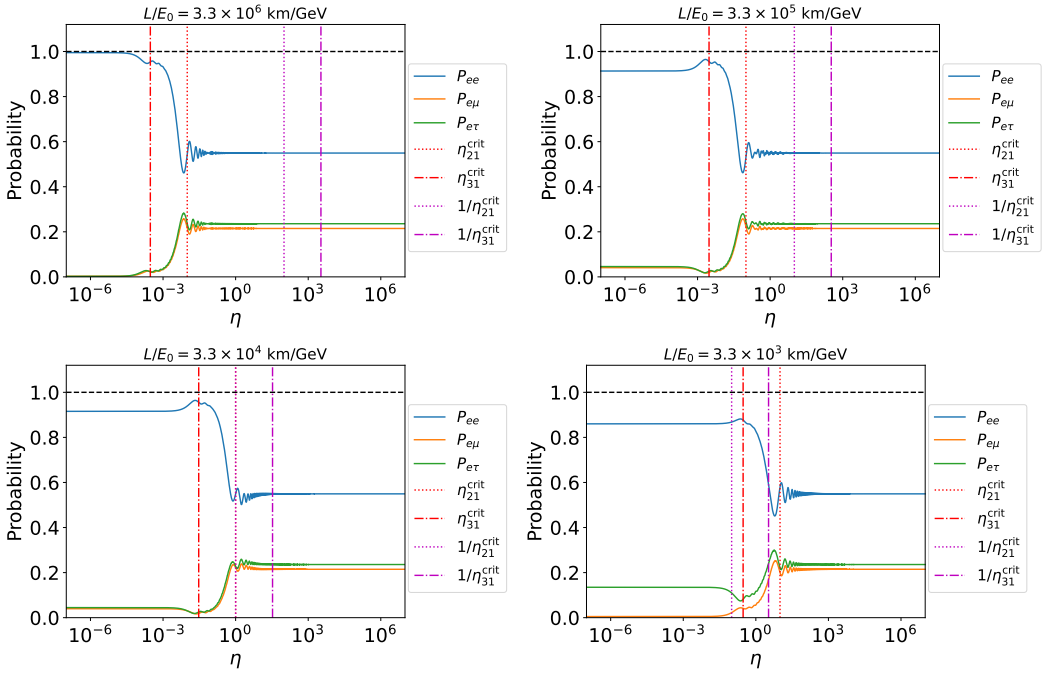


Figure 5. The transition probability when considering the energy bandwidth of a measurement. The neutrino spectrum follows a power law with index $p = 2$. The transition probability converges to $P_{\alpha\beta}^{\rm ave}$ at large η. The following oscillation parameters are adopted: $\Delta m_{21}^2 = 7.49 \times 10^{-5}\,{\rm eV}^2$, $\Delta m_{31}^2 = 2.513 \times 10^{-3}\,{\rm eV}^2$, $\theta_{12} = 33.68^\circ$, $\theta_{23} = 43.3^\circ$, $\theta_{13} = 8.56^\circ$, and $\delta_{\rm CP} = 212^\circ$ (NO) [1].

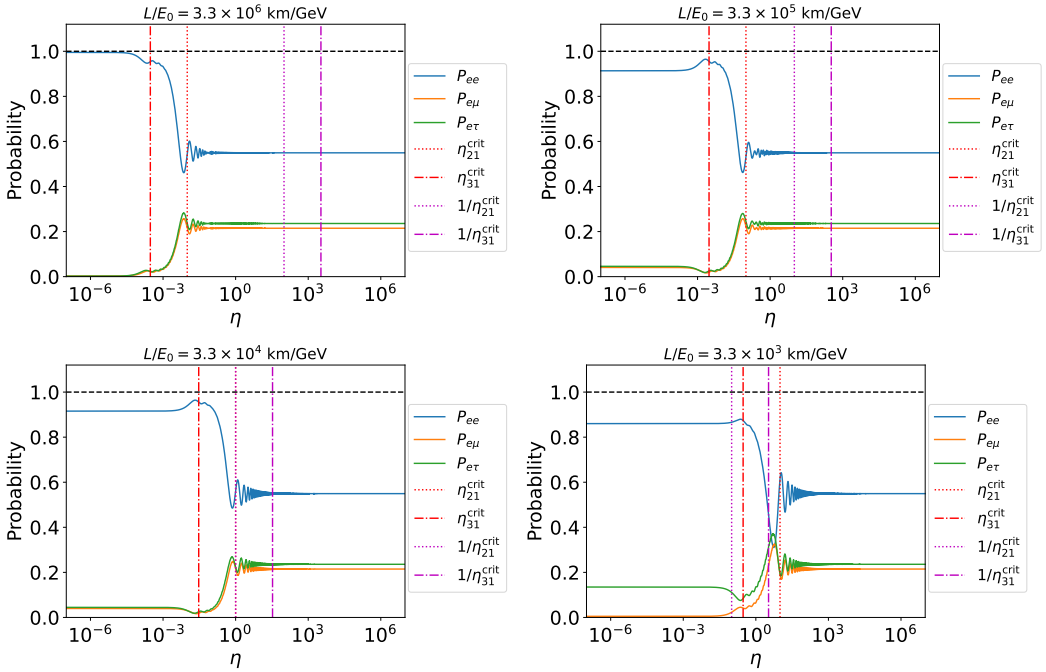


Figure 6. The transition probability when considering the energy bandwidth of a measurement. The neutrino spectrum follows a power law with index $p = 3$. The transition probability converges to $P_{\alpha\beta}^{\rm ave}$ at large η. The following oscillation parameters are adopted: $\Delta m_{21}^2 = 7.49 \times 10^{-5}\,{\rm eV}^2$, $\Delta m_{31}^2 = 2.513 \times 10^{-3}\,{\rm eV}^2$, $\theta_{12} = 33.68^\circ$, $\theta_{23} = 43.3^\circ$, $\theta_{13} = 8.56^\circ$, and $\delta_{\rm CP} = 212^\circ$ (NO) [1].

4. Implications on the Measurements of fLavour Ratio of Astrophysical Neutrinos

In Section 3, we analyse how the coherence length, the size of the emitter, the radial velocity of the source, and the limitations of measurements (detector size and energy bandwidth) affect the transition probability that we measure. Interestingly, all of them converge to the averaged transition probability under specific conditions. They can be summarised into five conditions (also summarised schematically in Figure 7):

1. The propagation length is much larger than the coherence length ($L \gg L_{jk}^{\rm coh}$).
2. The size of the emission zone is much larger than the oscillation length ($\Delta L \gg L_{jk}^{\rm osc}$).
3. The distance travelled by the source during the observation is much larger than the oscillation lengths ($v_r t_{\rm obs} \gg L_{jk}^{\rm osc}$).
4. The size of the detector is much larger than the oscillation length ($\Delta L \gg L_{jk}^{\rm osc}$).
5. The energy bandwidth of the data is sufficiently large ($\eta \gg \eta_{jk}^{\rm crit}$) and ideally the neutrino spectrum is steep.

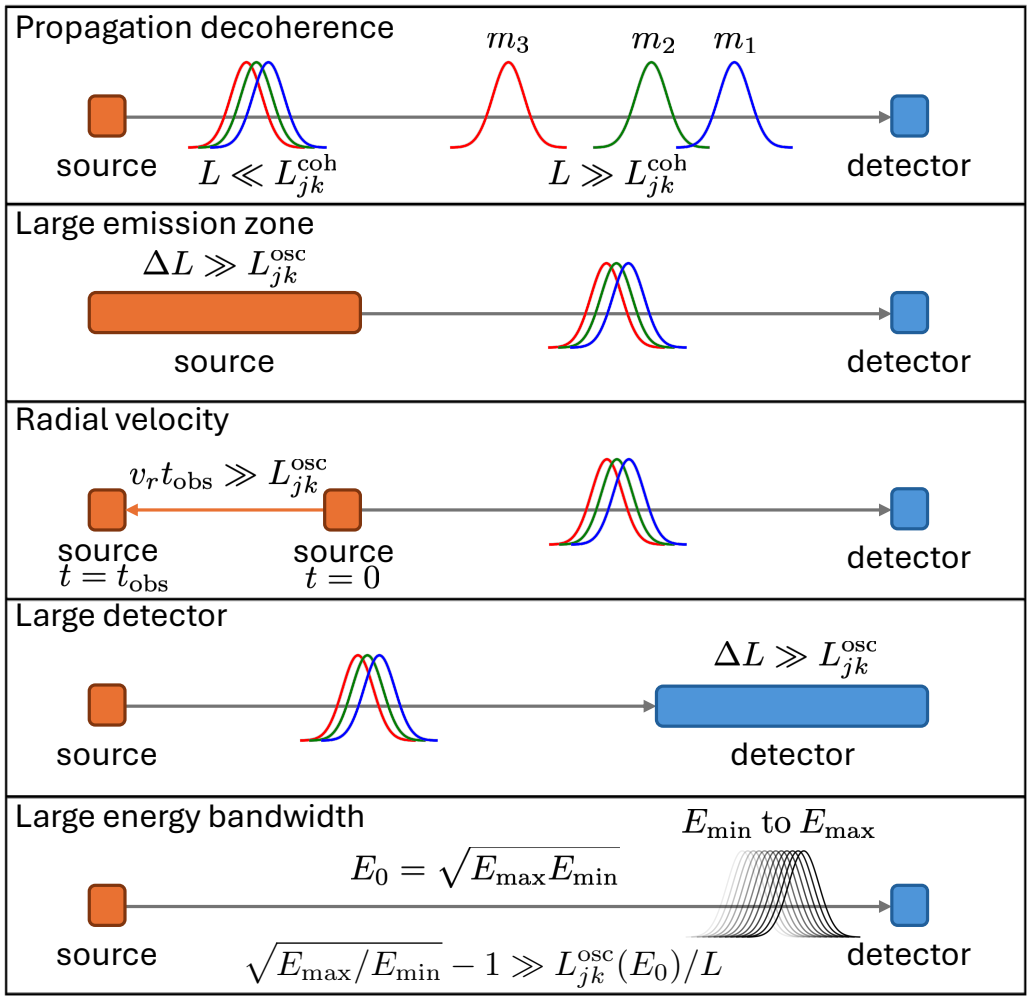


Figure 7. Schematic summary of the five conditions that would justify the averaged transition probability formula. From top to bottom are propagation decoherence ($L \gg L_{jk}^{\rm coh}$), large emission zone ($\Delta L \gg L_{jk}^{\rm osc}$), radial velocity ($v_r t_{\rm obs} \gg L_{jk}^{\rm osc}$), large detector ($\Delta L \gg L_{jk}^{\rm osc}$), and large energy bandwidth ($\eta \gg \eta_{jk}^{\rm crit}$). The energy-bandwidth condition $\eta \gg \eta_{jk}^{\rm crit}$ is rewritten into $\sqrt{E_{\rm max}/E_{\rm min}} - 1 \gg L_{jk}^{\rm osc}(E_0)/L$ to make the figure more self-explanatory.

If any one of these conditions is satisfied, the measured flavour ratio is expected to be consistent with the oscillation-averaged transition probability. While these conditions all

yield the same formula, their underlying physical origins are distinct. The first condition arises from a propagation effect, whereas the second is related to the properties of the source. The third condition results from a combination of source properties and experimental limitations, while the fourth and fifth conditions are essentially experimental in nature. The first two conditions can be regarded as intrinsic, in the sense that they are independent of the detector properties. If a system satisfies only the third, fourth, and/or fifth condition, it may in principle be possible to remove their influence by reducing the energy bandwidth, size of the detector, and observation time.

Once the validity of the averaged transition probability is established, the expected flavour composition at Earth can be readily obtained from any given initial flavour composition using Equation (5). When applying Equation (5), careful attention must be paid to the definition of the flavour ratio at the source. If the neutrino production site is free from neutrino interactions, the flavour ratio at the source is equivalent to the flavour ratio at production. If, however, neutrino interactions are non-negligible within or in the vicinity of the production site, the flavour ratio at the source should be taken as the flavour ratio at the point where the neutrinos have completely escaped the interacting region. For example, a neutrino produced at the core of the Sun is subject to matter effects during propagation through the solar interior, most notably the Mikheyev–Smirnov–Wolfenstein (MSW) effect [47]. In such cases, the flavour ratio at the source should be defined as the flavour ratio upon exit from the solar surface, where the neutrinos begin to propagate freely through space. Consequently, the neutrino flavour ratio to be substituted into Equation (5) may differ from the flavour ratio at the point of production.

Although the five conditions are derived under idealised assumptions, such as uniform emission and energy- and location-independent detection rates, they establish the minimal conditions that must be satisfied in order to apply the oscillation-averaged transition probability formula. In the following, we address two questions: Do astrophysical neutrinos typically satisfy one or more of these conditions? Does the oscillation-averaged transition probability remain applicable when the physical conditions deviate from those assumed in the idealised calculation? While high-energy astrophysical neutrinos produced in pion decay are the primary focus of this work, the analysis presented above is applicable to neutrino sources at any distance and across any energy scale. We extend our discussion to supernova neutrinos, which represent another major class of astrophysical neutrinos at lower energies (∼MeV), at the end of this section.

High-energy astrophysical neutrinos—NGC 1068 being the first static neutrino source detected by IceCube [11], we take its approximate distance and neutrino energy spectrum as the reference for our discussion below. High-energy astrophysical neutrinos are primarily produced in pion decay and muon decay. Neutrinos produced in the decay of these highly relativistic particles result in a wave packet of size $\sigma_x \sim \tau_\pi/\gamma_\pi \sim 10\,\mathrm{m}/\gamma_\pi$, or $\sigma_x \sim \tau_\mu/\gamma_\mu \sim 10^3\,\mathrm{m}/\gamma_\mu$ [43]. As shown in the right panel of Figure 1, most of the astrophysical sources remain in the coherent regime, though it is close to the transition region. For sources located beyond 1 Gpc, it is possible that the neutrinos they emit become incoherent when they reach the Earth, but that also depends on the energy of interest. Yet the incoherence may only affect the neutrinos from pion decay but not muon decay, as the latter has a wave packet size two orders of magnitude larger than the former. For high-energy neutrinos from NGC 1068, the incoherence of neutrino oscillation has little effect to the transition probability.

We next compare the sizes of the emitter and detector with the neutrino oscillation lengths. For TeV neutrinos, the oscillation lengths are $L_{21}^{\mathrm{osc}} \approx 3.3 \times 10^7\,\mathrm{km}\,(E/1\,\mathrm{TeV})$ and $L_{31}^{\mathrm{osc}} \approx 10^6\,\mathrm{km}\,(E/1\,\mathrm{TeV})$. Even for large-scale detectors such as IceCube, the physical extent is only ∼1 km, which is many orders of magnitude smaller than the oscillation lengths. The

size of the emission zone is considerably more uncertain, and different models may predict vastly different values. In the case of NGC 1068, the inferred size of the emission zone spans the range 10^8–10^{12} km across different models (e.g., [48–51]), which is at least comparable to, and potentially much larger than, the relevant oscillation lengths. Nevertheless, the degree of uniformity of the emission within the emitting zone is poorly constrained. Given the large uncertainties in the properties of the emission zone, this condition does not constitute the most robust argument for applying the oscillation-averaged transition probability.

NGC 1068 was confirmed as a neutrino point source only after accumulating over ten years of data [11]. Located at redshift $z \approx 0.0038$, NGC 1068 has a recession velocity of $v_r \approx 1100\,\mathrm{km\,s^{-1}}$ [52]. Over an observation period of ten years, the source recedes by $\Delta L \sim 3.5\times10^{11}$ km $(t_{\rm obs}/10\,\mathrm{yr})$, which far exceeds the relevant oscillation lengths. To suppress this effect, the observation duration would need to be reduced to no more than a few hours, which is not feasible given the detection rates of current detectors such as IceCube. The combination of the recession velocity and the required exposure time therefore provides a robust justification for the use of the oscillation-averaged transition probability.

Finally, we examine the energy bandwidth condition. For a source at a distance of 10 Mpc emitting primarily at TeV energies, the critical η are $\eta_{21}^{\rm crit} \sim 10^{-13}\,(E/1\,\mathrm{TeV})(L/10\,\mathrm{Mpc})^{-1}$ and $\eta_{31}^{\rm crit} \sim 10^{-14}\,(E/1\,\mathrm{TeV})(L/10\,\mathrm{Mpc})^{-1}$. The typical range of η for current neutrino detectors is of order 1–100, which lies significantly above $\eta_{jk}^{\rm crit}$ and well below $1/\eta_{jk}^{\rm crit}$. Therefore, for any smooth neutrino energy spectrum, such as a power law, it is reasonable to expect that the measured transition probability is well approximated by the oscillation-averaged transition probability. For example, the neutrino spectrum of NGC 1068 can be described by a power law with index $p \sim 3.2$–3.4 [11,53], and thus a neutrino flavour ratio study of NGC 1068 with $\eta \sim 1$–10 is expected to be consistent with the averaged transition probability.

In summary, high-energy astrophysical neutrinos likely remain coherent upon arrival at the detector, but may not hold for those originated beyond Gpc distance. Given that the properties of the emission regions are highly uncertain, any arguments that rely on the properties of the emission regions may not be considered as a strong argument. Lastly, the cosmological recession velocity and the energy bandwidth arguments provide valid justifications for the use of the averaged transition probability for NGC 1068, and most of the extragalactic sources.

Supernova neutrinos—We consider a Galactic supernova event producing primarily MeV-scale neutrinos, which represents a principal target for the Hyper-Kamiokande detector. As discussed above, neutrinos produced in supernovae have small wave packets owing to the dense environment of the progenitor. Depending on the model, the wave packet size ranges from 10^{-16} m to 10^{-11} m [36,38,44,45]. The corresponding coherence lengths are

$$L_{31}^{\rm coh} \approx 2\,\mathrm{km}\left(\frac{E}{1\,\mathrm{MeV}}\right)^2\left(\frac{\sigma_x}{1\,\mathrm{pm}}\right), \tag{12}$$

$$L_{21}^{\rm coh} \approx 75\,\mathrm{km}\left(\frac{E}{1\,\mathrm{MeV}}\right)^2\left(\frac{\sigma_x}{1\,\mathrm{pm}}\right). \tag{13}$$

Since the distance to even the nearest potential Galactic supernova far exceeds these coherence lengths, supernova neutrinos are guaranteed to arrive at the detector in an incoherent state.

One assumption underlying the model presented in Section 3.2 is that the emission zone is transparent to neutrinos. During a supernova, however, the environment is extremely dense, and neutrinos undergo significant interactions with both matter and other neutrinos [54]. This substantially complicates the picture, and the model we presented may not adequately capture the physical conditions within a supernova environment. Consequently, the emission properties of supernova neutrinos do not provide a reliable basis for applying the oscillation-averaged transition probability. The production and transport

of supernova neutrinos is a complex process and we refer the reader to Refs. [54,55] for further details.

Stars in the Milky Way have typical radial velocities of order 10–100 km s^{-1}. Assuming that the radial velocity does not change significantly at the onset of the supernova, we adopt the stellar radial velocity as a proxy for the radial velocity of the supernova. The duration of significant neutrino emission is of order 10 ms to 10 s [54], such that

$$v_r t_{\rm obs} \sim 0.1\,{\rm km}\left(\frac{v_r}{10\,{\rm km\,s^{-1}}}\right)\left(\frac{t_{\rm obs}}{10\,{\rm ms}}\right) \sim 10^3\,{\rm km}\left(\frac{v_r}{100\,{\rm km\,s^{-1}}}\right)\left(\frac{t_{\rm obs}}{10\,{\rm s}}\right). \tag{14}$$

For comparison, the oscillation lengths of MeV neutrinos are $L_{21}^{\rm osc} \approx 33\,{\rm km}\,(E/1\,{\rm MeV})$ and $L_{31}^{\rm osc} \approx 1\,{\rm km}\,(E/1\,{\rm MeV})$. Whether the travelled distance accumulated during the observation exceeds the oscillation lengths therefore depends sensitively on the radial velocity of the progenitor star, the duration of the neutrino burst, and the neutrino energy.

Lastly, we examine the energy bandwidth condition. Given $E = 1\,{\rm MeV}$ and $L = 10\,{\rm kpc}$, we obtain $\eta_{21}^{\rm crit} \sim 10^{-16}(E/1\,{\rm MeV})(L/10\,{\rm kpc})^{-1}$ and $\eta_{31}^{\rm crit} \sim 10^{-17}(E/1\,{\rm MeV})(L/10\,{\rm kpc})^{-1}$. Due to the small critical values, the energy bandwidth argument can also justify the averaged transition probability. In conclusion, the averaged transition probability is intrinsically correct for supernova neutrinos due to incoherence, while the radial velocity and energy bandwidth argument might further support such an approximation.

5. Conclusions

The measured flavour ratio of high-energy astrophysical neutrinos ($\gtrsim$ GeV) is expected to be close to equipartition. This expectation rests on two widely adopted assumptions: (1) astrophysical neutrinos are predominantly produced via pion and muon decays, and (2) the measured transition probability can be well approximated by the oscillation-averaged transition probability. The commonly invoked justifications for the second assumption include the large distances to the sources and the limited energy resolution of detectors. While these justifications are valid to a certain extent, particularly within the parameter space relevant to astrophysical neutrino experiments, the conditions under which they hold are seldom quantified. In this work, we quantified in detail the conditions required for the oscillation-averaged transition probability to be applicable, encompassing the neutrino wave packet size, the production mechanism, the neutrino energy, the propagation distance, the energy spectrum of the source, and the detector specifications. For the oscillation-averaged transition probability to be applicable, the source or the measurement must satisfy at least one of the following conditions:

1. The length of propagation is much larger than the coherence length ($L \gg L_{jk}^{\rm coh}$).
2. The size of the emitter is much larger than the oscillation length ($\Delta L \gg L_{jk}^{\rm osc}$).
3. The radial distance travelled by the source during an observation is much larger than the oscillation lengths ($v_r t_{\rm obs} \gg L_{jk}^{\rm osc}$).
4. The size of the detector is much larger than the oscillation length ($\Delta L \gg L_{jk}^{\rm osc}$).
5. The energy bandwidth of the experiment is sufficiently large ($\eta \gg \eta_{jk}^{\rm crit}$) and ideally the neutrino spectrum is steep.

Although the present work focuses primarily on high-energy astrophysical neutrinos, with a brief discussion of supernova neutrinos, the analysis is broadly applicable to most neutrino-emitting systems, including atmospheric, reactor, and accelerator neutrinos. Researchers can apply the conditions derived above to their own systems of interest and assess whether the transition probability may be modified by any of these factors.

Among many factors, we summarise below some of the most promising factors that assure the validity of the averaged transition probability. In the context of high-energy astrophysical neutrino experiments, the large distances to the sources result in small values

of $\eta^{\rm crit}$, and we demonstrate that the energy bandwidth of the data typically provides a robust justification for the oscillation-averaged approximation. Furthermore, given the long exposure time required to confirm a neutrino source, the oscillation-averaged transition probability can also be justified for most TeV extragalactic neutrino sources on the basis of the cosmological recession velocity, assuming an exposure time of ∼10 yr. In cases where the neutrino wave packet is small, as in supernova neutrinos, the propagation length may exceed the coherence length, such that neutrinos arrive at the detector in an incoherent state. In this regime, the measured transition probability is intrinsically equal to the oscillation-averaged value, rather than being a consequence of experimental limitations—a key distinction from the arguments presented above. This work provides a systematic and quantitative account of the conditions that must be satisfied in order to apply the oscillation-averaged transition probability, thereby establishing a rigorous foundation for future flavour ratio studies seeking to identify deviations from this standard prediction.

Funding: This research received no external funding.

Data Availability Statement: The original contributions presented in this study are included in the article. Further inquiries can be directed to the corresponding author.

Acknowledgments: I thank Jane Sinan Long for proofreading the manuscript and providing valuable comments. I thank Ming-Chung Chu for the useful scientific discussion related to this manuscript. During the preparation of this manuscript, the author used ChatGPT GPT-6 to improve the readability of the text. The authors have reviewed and edited the output and take full responsibility for the content of this publication.

Conflicts of Interest: The author declares no conflicts of interest.

Appendix A. Further Analysis of the Results in Section 3.3

In this appendix, we will explain Equation (11) and the results shown in Figure 4 analytically and graphically. First, we express explicitly the integral in Equation (11):

$$\begin{aligned}\langle P_{\alpha\beta}(L,E_0)\rangle^{\rm uni}_{\Delta E} &= \delta_{\alpha\beta} - 4\sum_{j>k}\Re(U^*_{\alpha j}U_{\beta j}U_{\alpha k}U^*_{\beta k})\frac{1}{\Delta E}\int_{E_{\rm min}}^{E_{\rm max}}{\rm d}E\,\sin^2\left(\frac{\Delta m^2_{jk}L}{4E}\right)\\ &\quad + 2\sum_{j>k}\Im(U^*_{\alpha j}U_{\beta j}U_{\alpha k}U^*_{\beta k})\frac{1}{\Delta E}\int_{E_{\rm min}}^{E_{\rm max}}{\rm d}E\,\sin\left(\frac{\Delta m^2_{jk}L}{2E}\right) \qquad \text{(A1)}\\ &= \delta_{\alpha\beta}\\ &\quad - 4\sum_{j>k}\Re(U^*_{\alpha j}U_{\beta j}U_{\alpha k}U^*_{\beta k})\frac{1}{\Delta E}\left[E\sin^2\left(\frac{\Delta m^2_{jk}L}{4E}\right) - \frac{\Delta m^2_{jk}L}{4}{\rm Si}\left(\frac{\Delta m^2_{jk}L}{2E}\right)\right]_{E=E_{\rm min}}^{E=E_{\rm max}}\\ &\quad + 2\sum_{j>k}\Im(U^*_{\alpha j}U_{\beta j}U_{\alpha k}U^*_{\beta k})\frac{1}{\Delta E}\left[E\sin\left(\frac{\Delta m^2_{jk}L}{2E}\right) - \frac{\Delta m^2_{jk}L}{2}{\rm Ci}\left(\frac{\Delta m^2_{jk}L}{2E}\right)\right]_{E=E_{\rm min}}^{E=E_{\rm max}}, \qquad \text{(A2)}\end{aligned}$$

where ${\rm Si}(x)$ is the sine integral and ${\rm Ci}(x)$ is the cosine integral. In the small-η or small-ΔE limit, Equation (A1) recovers the standard oscillation formula. In the large-η or large-ΔE limit, we have $E_{\rm max}\to\infty$ and $E_{\rm min}\to 0$ such that $E_{\rm max}/\Delta E\approx 1$. Given that ${\rm Si}(x\to 0)\approx x$, ${\rm Si}(x\to\infty)\approx \pi/2-(\cos x)/x$, ${\rm Ci}(x\to 0)\approx \gamma+\ln(x)$ ($\gamma\approx 0.577$ is the Euler's constant), and ${\rm Ci}(x\to\infty)\approx(\sin x)/x$, all the terms in Equation (A2) except for the Kronecker delta function vanish. The result is harder to interpret from the equation when η is at moderate values, and we take a graphical approach below.

The behaviour of the result depends on the region over which the integral of the sine and sine-squared functions in Equation (A1) is evaluated. This can be understood graphically, as illustrated in Figure A1, where the shaded regions represent the distinct regimes over

which the integral in Equation (A1) is evaluated. The green region corresponds to the small-η limit. Since the integration interval is small, the integrated value essentially reflects the local value of the integrand. The blue region corresponds to the large-η limit. Since the integral is dominated by the tail of $\sin(1/x)$, whose values approach zero for large x, the integral also vanishes in this limit. The red region represents the regime $\eta_{jk}^{\text{crit}} < \eta < 1/\eta_{jk}^{\text{crit}}$, in which $\sin(1/x)$ behaves similarly to a standard sinusoidal function, such that the integral approaches zero for the sine function and $1/2$ for the sine-squared function. The yellow region represents the regime $1/\eta_{jk}^{\text{crit}} < \eta < \eta_{jk}^{\text{crit}}$, in which part of the integration spans the oscillating regime while the remainder falls within the tail of $\sin(1/x)$. Since these two contributions compete with one another, the integral does not converge to a well-defined value. These shaded regions correspond to those in Figure A2, which shows the associated transition probability.

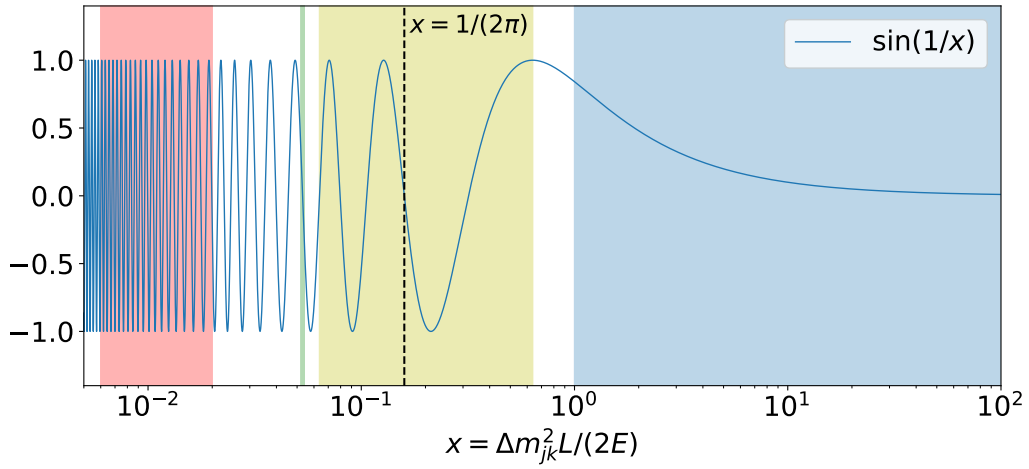


Figure A1. The blue curve shows the $\sin(1/x)$ function. The shaded areas represent different distinct regimes where the integral in Equation (A1) takes place. The green area represents the small η limit, the blue area represents the large η limit, the red area represents the regime where $\eta_{jk}^{\text{crit}} < \eta < 1/\eta_{jk}^{\text{crit}}$, and the yellow area represents the regime where $1/\eta_{jk}^{\text{crit}} < \eta < \eta_{jk}^{\text{crit}}$. These shaded areas correspond to the shaded area in Figure A2.

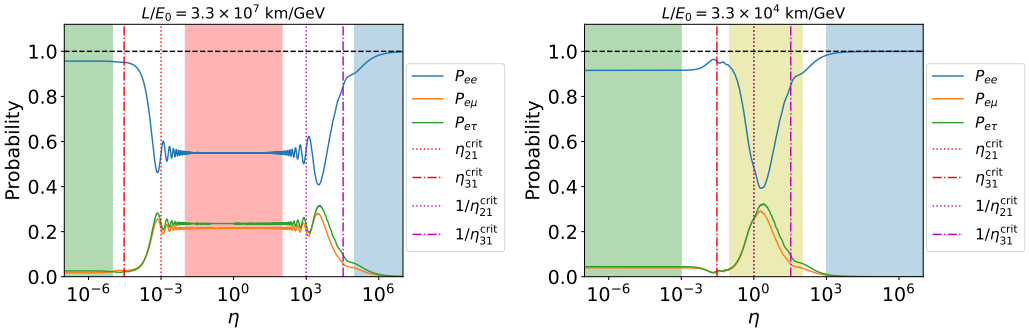


Figure A2. The transition probability when considering the energy resolution of the detector. The left and right panels are the same as Figure 4a,d, respectively, except that regions are shaded in different colours. The green and blue areas represent the small and large η limit, respectively. The red and yellow areas represents the regime where $\eta_{jk}^{\text{crit}} < \eta < 1/\eta_{jk}^{\text{crit}}$ and $1/\eta_{jk}^{\text{crit}} < \eta < \eta_{jk}^{\text{crit}}$, respectively. These shaded areas correspond to the shaded area in Figure A1.

Notes

[1] In neutrino observations, because of the low detection rate of neutrinos, data are usually integrated over a wide energy range that exceeds the energy resolution of a single event. Therefore, this factor depends on how data are processed rather than the intrinsic property of a detector.

References

1. Esteban, I.; Gonzalez-Garcia, M.C.; Maltoni, M.; Martinez-Soler, I.; Pinheiro, J.P.; Schwetz, T. NuFit-6.0: Updated global analysis of three-flavor neutrino oscillations. *J. High Energy Phys.* **2024**, *2024*, 216. [CrossRef]
2. Abbasi, R. et al. [IceCube Collaboration] Characterization of the Three-Flavor Composition of Cosmic Neutrinos with IceCube. *Phys. Rev. Lett.* **2026**, *137*, 081002. [CrossRef] [PubMed]
3. An, F.P. et al. [Daya Bay Collaboration] Precision Measurement of Reactor Antineutrino Oscillation at Kilometer-Scale Baselines by Daya Bay. *Phys. Rev. Lett.* **2023**, *130*, 161802. [CrossRef] [PubMed]
4. Abreu, M. et al. [SNO+Collaboration] Measurement of Reactor Antineutrino Oscillation at SNO+. *Phys. Rev. Lett.* **2025**, *135*, 121801. [CrossRef] [PubMed]
5. The NOvA Collaboration; The T2K Collaboration. Joint neutrino oscillation analysis from the T2K and NOvA experiments. *Nature* **2025**, *646*, 818–824. [CrossRef] [PubMed]
6. Agostini, M. et al. [Borexino Collaboration] Simultaneous precision spectroscopy of *pp*, ^{7}Be, and *pep* solar neutrinos with Borexino Phase-II. *Phys. Rev. D* **2019**, *100*, 082004. [CrossRef]
7. Agostini, M. et al. [Borexino Collaboration] Improved measurement of ^{8}B solar neutrinos with 1.5 kt · y of Borexino exposure. *Phys. Rev. D* **2020**, *101*, 062001. [CrossRef]
8. Allega, A. et al. [SNO+Collaboration] Measurement of the ^{8}B solar neutrino flux using the full SNO+ water phase dataset. *Phys. Rev. D* **2024**, *110*, 122003. [CrossRef]
9. Abe, K. et al. [Super-Kamiokande Collaboration] Solar neutrino measurements using the full data period of Super-Kamiokande-IV. *Phys. Rev. D* **2024**, *109*, 092001. [CrossRef]
10. D'Ammando, F. et al. [IceCube Collaboration] Multimessenger observations of a flaring blazar coincident with high-energy neutrino IceCube-170922A. *Science* **2018**, *361*, eaat1378. [CrossRef] [PubMed]
11. Abbasi, R. et al. [IceCube Collaboration] Evidence for neutrino emission from the nearby active galaxy NGC 1068. *Science* **2022**, *378*, 538–543. [CrossRef] [PubMed]
12. Abbasi, R. et al. [IceCube Collaboration] Observation of high-energy neutrinos from the Galactic plane. *Science* **2023**, *380*, 1338–1343. [CrossRef] [PubMed]
13. Abe, K. et al. [Super-Kamiokande Collaboration] Diffuse supernova neutrino background search at Super-Kamiokande. *Phys. Rev. D* **2021**, *104*, 122002. [CrossRef]
14. Aartsen, M.G.; Abbasi, R.; Ackermann, M.; Adams, J.; Aguilar, J.A.; Ahlers, M.; Ahrens, M.; Alispach, C.; Allison, P.; Amin, N.M.; et al. IceCube-Gen2: The window to the extreme Universe. *J. Phys. G Nucl. Phys.* **2021**, *48*, 060501. [CrossRef]
15. Aiello, S.; et al. [KM3NeT Collaboration] Astronomy potential of KM3NeT/ARCA. *Eur. Phys. J. C* **2024**, *84*, 885. [CrossRef]
16. Avrorin, A.D.; Avrorin, A.V.; Aynutdinov, V.M.; Bannash, R.; Belolaptikov, I.A.; Brudanin, V.B.; Budnev, N.M.; Domogatsky, G.V.; Doroshenko, A.A.; Dvornicky, R.; et al. Neutrino Telescope in Lake Baikal: Present and Future. *arXiv* **2019**, arXiv:1908.05427.
17. Agostini, M.; Böhmer, M.; Bosma, J.; Clark, K.; Danninger, M.; Fruck, C.; Gernhäuser, R.; Gärtner, A.; Grant, D.; Henningsen, F.; et al. The Pacific Ocean Neutrino Experiment. *Nat. Astron.* **2020**, *4*, 913–915. Correction in *Nat. Astron.* **2020**, *4*, 1111. [CrossRef]
18. Huang, T.Q.; Cao, Z.; Chen, M.; Liu, J.; Wang, Z.; You, X.; Qi, Y. Proposal for the High Energy Neutrino Telescope. In Proceedings of the 38th International Cosmic Ray Conference, Nagoya, Japan, 26 July–3 August 2024; p. 1080.
19. Ye, Z.P.; Hu, F.; Tian, W.; Chang, Q.C.; Chang, Y.L.; Cheng, Z.S.; Gao, J.; Ge, T.; Gong, G.H.; Guo, J.; et al. A multi-cubic-kilometre neutrino telescope in the western Pacific Ocean. *Nat. Astron.* **2023**, *7*, 1497–1505. [CrossRef]
20. Zhang, H.; Cui, Y.; Huang, Y.; Lin, S.; Liu, Y.; Qiu, Z.; Shao, C.; Shi, Y.; Xie, C.; Yang, L. A proposed deep sea Neutrino Observatory in the Nanhai. *arXiv* **2024**, arXiv:2408.05122. [CrossRef]
21. Abe, K.; Abe, K.; Aihara, H.; Aimi, A.; Akutsu, R.; Andreopoulos, C.; Anghel, I.; Anthony, L.H.; Antonova, M.; Ashida, Y.; et al. Hyper-Kamiokande Design Report. *arXiv* **2018**, arXiv:1805.04163. [CrossRef]
22. Abbasi, R. et al. [IceCube Collaboration] Search for quantum gravity using astrophysical neutrino flavour with IceCube. *Nat. Phys.* **2022**, *18*, 1287–1292. [CrossRef]
23. Bustamante, M.; Ellis, J.; Konoplich, R.; Sakharov, A.S. Probing Lorentz invariance with a high-energy neutrino flare. *Phys. Rev. D* **2025**, *111*, 123031. [CrossRef]
24. Oikonomou, F.; Murase, K.; Padovani, P.; Resconi, E.; Mészáros, P. High-energy neutrino flux from individual blazar flares. *Mon. Not. R. Astron. Soc.* **2019**, *489*, 4347–4366. [CrossRef]

25. Fang, K.; Gallagher, J.S.; Halzen, F. The TeV Diffuse Cosmic Neutrino Spectrum and the Nature of Astrophysical Neutrino Sources. *Astrophys. J.* **2022**, *933*, 190. [CrossRef]
26. Rodrigues, X. Neutrinos from extreme astrophysical sources. *New Astron. Rev.* **2026**, *102*, 101747. [CrossRef]
27. Winter, W.; Fiorillo, D.F.G.; Buson, S. Single-source-class interpretation of the diffuse astrophysical neutrino flux. *Phys. Rev. D* **2026**, *113*, 123043. [CrossRef]
28. Hümmer, S.; Maltoni, M.; Winter, W.; Yaguna, C. Energy dependent neutrino flavor ratios from cosmic accelerators on the Hillas plot. *Astropart. Phys.* **2010**, *34*, 205–224. [CrossRef]
29. Baerwald, P.; Hümmer, S.; Winter, W. Magnetic field and flavor effects on the gamma-ray burst neutrino flux. *Phys. Rev. D* **2011**, *83*, 067303. [CrossRef]
30. Riabtsev, K.; Troitsky, S. Energy-dependent flavor ratios, cascade/track spectrum tension and high-energy neutrinos from magnetospheres of supermassive black holes. *Phys. Lett. B* **2023**, *839*, 137758. [CrossRef]
31. Coleman, A.; Ericsson, O.; Glaser, C.; Bustamante, M. Flavor composition of ultrahigh-energy cosmic neutrinos: Measurement forecasts for in-ice radio-based EeV neutrino telescopes. *Phys. Rev. D* **2024**, *110*, 023044. [CrossRef]
32. Argüelles, C.A.; Katori, T.; Salvado, J. Effect of New Physics in Astrophysical Neutrino Flavor. *Phys. Rev. Lett.* **2015**, *115*, 161303. [CrossRef] [PubMed]
33. Bustamante, M.; Beacom, J.F.; Murase, K. Testing decay of astrophysical neutrinos with incomplete information. *Phys. Rev. D* **2017**, *95*, 063013. [CrossRef]
34. Rasmussen, R.W.; Lechner, L.; Ackermann, M.; Kowalski, M.; Winter, W. Astrophysical neutrinos flavored with beyond the Standard Model physics. *Phys. Rev. D* **2017**, *96*, 083018. [CrossRef]
35. Barger, V.; Marfatia, D.; Whisnant, K. *The Physics of Neutrinos*; Princeton University Press: Princeton, NJ, USA, 2013.
36. Giunti, C.; Chung, W.K. *Fundamentals of Neutrino Physics and Astrophysics*; Oxford University Press: Oxford, UK, 2007.
37. Bustamante, M.; Beacom, J.F.; Winter, W. Theoretically Palatable Flavor Combinations of Astrophysical Neutrinos. *Phys. Rev. Lett.* **2015**, *115*, 161302. [CrossRef] [PubMed]
38. Kersten, J.; Smirnov, A.Y. Decoherence and oscillations of supernova neutrinos. *Eur. Phys. J. C* **2016**, *76*, 339. [CrossRef]
39. Ahlers, M.; Helbing, K.; Pérez de los Heros, C. Probing particle physics with IceCube. *Eur. Phys. J. C* **2018**, *78*, 924. [CrossRef]
40. Song, N.; Li, S.W.; Argüelles, C.A.; Bustamante, M.; Vincent, A.C. The future of high-energy astrophysical neutrino flavor measurements. *J. Cosmol. Astropart. Phys.* **2021**, *2021*, 054. [CrossRef]
41. Akhmedov, E.; Smirnov, A.Y. Damping of neutrino oscillations, decoherence and the lengths of neutrino wave packets. *J. High Energy Phys.* **2022**, *2022*, 82. [CrossRef]
42. Kim, C.W. Neutrino physics: Fundamentals of neutrino oscillations. *J. Korean Phys. Soc.* **1996**, *29*, S157–S166. [CrossRef]
43. Akhmedov, E.K.; Hernandez, D.; Smirnov, A.Y. Neutrino production coherence and oscillation experiments. *J. High Energy Phys.* **2012**, *2012*, 52. [CrossRef]
44. Anada, H.; Nishimura, H. Neutrino vacuum oscillation and neutrino burst from SN1987A. *Phys. Rev. D* **1988**, *37*, 552–554. [CrossRef] [PubMed]
45. Anada, H.; Nishimura, H. Coherence condition for resonant neutrino oscillation. *Phys. Rev. D* **1990**, *41*, 2379–2383. [CrossRef] [PubMed]
46. Smolsky, J.; Leach, K.G.; Abells, R.; Amaro, P.; Andoche, A.; Borbridge, K.; Bray, C.; Cantor, R.; Diercks, D.; Fretwell, S.; et al. Direct experimental constraints on the spatial extent of a neutrino wavepacket. *Nature* **2025**, *638*, 640–644. [CrossRef] [PubMed]
47. Mikheev, S.P.; Smirnov, A.I. Resonant amplification of ν oscillations in matter and solar-neutrino spectroscopy. *Il Nuovo Cimento CC* **1986**, *9*, 17–26. [CrossRef]
48. Fang, K.; Lopez Rodriguez, E.; Halzen, F.; Gallagher, J.S. High-energy Neutrinos from the Inner Circumnuclear Region of NGC 1068. *Astrophys. J.* **2023**, *956*, 8. [CrossRef]
49. Fiorillo, D.F.G.; Petropoulou, M.; Comisso, L.; Peretti, E.; Sironi, L. TeV Neutrinos and Hard X-Rays from Relativistic Reconnection in the Corona of NGC 1068. *Astrophys. J. Lett.* **2024**, *961*, L14. [CrossRef]
50. Saurenhaus, L.; Capel, F.; Oikonomou, F.; Buchner, J. Constraining the contribution of Seyfert galaxies to the diffuse neutrino flux in light of point source observations. *Phys. Rev. D* **2026**, *113*, 023019. [CrossRef]
51. Das, A.; Murase, K.; Zhang, B.T. Multimessenger Constraints on Production Sites of High-Energy Neutrinos from NGC 1068. *arXiv* **2026**, arXiv:2604.01222. [CrossRef]
52. Bland-Hawthorn, J.; Gallimore, J.F.; Tacconi, L.J.; Brinks, E.; Baum, S.A.; Antonucci, R.R.J.; Cecil, G.N. The Ringberg Standards for NGC 1068. *Astrophys. Space Sci.* **1997**, *248*, 9–19. [CrossRef]
53. Abbasi, R. et al. [IceCube Collaboration] Evidence for Neutrino Emission from X-Ray-bright Active Galactic Nuclei with IceCube. *Astrophys. J. Lett.* **2026**, *1000*, L26. [CrossRef]

54. Mirizzi, A.; Tamborra, I.; Janka, H.T.; Saviano, N.; Scholberg, K.; Bollig, R.; Hüdepohl, L.; Chakraborty, S. Supernova neutrinos: Production, oscillations and detection. *Riv. Nuovo Cimento* **2016**, *39*, 1–112. [CrossRef]
55. Janka, H.T. Neutrino Emission from Supernovae. In *Handbook of Supernovae*; Alsabti, A.W., Murdin, P., Eds.; Springer International Publishing AG: Cham, Switzerland, 2017; p. 1575. [CrossRef]

Disclaimer/Publisher's Note: The statements, opinions and data contained in all publications are solely those of the individual author(s) and contributor(s) and not of MDPI and/or the editor(s). MDPI and/or the editor(s) disclaim responsibility for any injury to people or property resulting from any ideas, methods, instructions or products referred to in the content.